NSRRC -Jo 4748 (2015)

THE JOURNAL OF CHEMICAL PHYSICS 142, 214905 (2015)

Hierarchical self-assembly of nanoparticles in polymer matrix and the nature of the interparticle interaction

Yu-Chiao Lin,[1] Chun-Yu Chen,[2] Hsin-Lung Chen,[1,a)] Takeji Hashimoto,[1,3,a)]
Show-An Chen,[1] and Yen-Cheng Li[4]
[1]*Department of Chemical Engineering and Frontier Research Center on Fundamental and Applied Sciences of Matters, National Tsing Hua University, Hsinchu 30013, Taiwan*
[2]*National Synchrotron Radiation Research Center, Hsinchu 300, Taiwan*
[3]*Quantum Beam Science Center, Japan Atomic Energy Agency, Tokai-mura, Naka-gun, Ibaraki 319-1195, Japan and Kyoto University, Kyoto 606-6501, Japan*
[4]*Material and Chemical Research Laboratories, Industrial Technology Research Institute, Hsinchu 300, Taiwan*

(Received 15 March 2015; accepted 11 May 2015; published online 3 June 2015)

Using small angle X-ray scattering (SAXS), we elucidated the spatial organization of palladium (Pd) nanoparticles (NPs) in the polymer matrix of poly(2-vinylpyridine) (P2VP) and the nature of inter-nanoparticle interactions, where the NPs were synthesized in the presence of P2VP by the reduction of palladium acetylacetonate ($Pd(acac)_2$). The experimental SAXS profiles were analysed on the basis of a hierarchical structure model considering the following two types of interparticle potential: (i) hard-core repulsion only (i.e., the hard-sphere interaction) and (ii) hard-core repulsion together with an attractive potential well (i.e., the sticky hard-sphere interaction). The corresponding theoretical scattering functions, which were used for analysing the experimental SAXS profiles, were obtained within the context of the Percus-Yevick closure and the Ornstein-Zernike equation in the fundamental liquid theory. The analyses revealed that existence of the attractive potential well is indispensable to account for the experimental SAXS profiles. Moreover, the morphology of the hybrids was found to be characterized by a hierarchical structure with three levels, where about six primary NPs with the diameter of ca. 1.8 nm (level one) formed local clusters (level two), and these clusters aggregated to build up a large-scale mass-fractal structure (level three) with the fractal dimension of ca. 2.3. The scattering function developed here is of general use for quantitatively characterizing the morphological structures of polymer/NP hybrids and, in particular, for exploring the interaction potential of the NPs on the basis of the fundamental liquid theory. © *2015 AIP Publishing LLC.* [http://dx.doi.org/10.1063/1.4921567]

I. INTRODUCTION

Controlling the spatial distributions of nanoparticles (NPs) in polymer matrices is an important fundamental physical problem in polymer-based nanohybrids and in polymer physics as well. In this work, we aimed at elucidating the nature of inter-nanoparticle interaction which is the most important and basic parameter governing the spatial distribution of the NPs in the polymer matrices. For this purpose, we used a scattering method which is indispensable for resolving (i) the inter-nanoparticle interaction potential on the basis of the fundamental theories for liquid state of atoms and/or particles and (ii) the hierarchical assembly of the NPs in the polymer matrices. The nanohybrids studied in this work were synthesized by a thermal reduction of a metal salt homogeneously dissolved in a polymer matrix.

The combination of inorganic NP and polymer to form hybrids has attracted extensive interests for enhancing polymer properties or seeking a balance or synergy of the constituent properties under low inorganic filler contents.[1–3] The morphological structure characterized by the dispersion state of the NPs in the polymer matrix and the structure of the NP-polymer interface are the key parameters governing the hybrid properties.[3–8] A uniform dispersion of NPs is often desirable for achieving effective mechanical reinforcement, while percolated structures for constructing continuous conductive paths of the NP fillers are essential for enhancing the electrical and thermal conductivities of the hybrids.[9–12]

In spite of the extensive efforts in developing polymer/NP hybrids, the systematic control of the dispersion morphology of the NPs in the polymer matrix, which is of primary importance for tuning the hybrid properties, still remains a challenging task. A major barrier lies in the general lack of quantitative understanding of the NP dispersion morphology over a broad range of length scale and the nature of the interparticle interaction in the polymer matrices. These fundamental informations are indeed essential for elucidating the roles of various physical factors governing the structure and properties of the hybrids, including NP-polymer interaction at their interface and interfacial structure, kinetics of NP aggregation, thermodynamics of the NP/polymer mixture, and the kinetics of a gas-liquid phase separation of NPs in the polymer matrices.

Block copolymers (bcps) have been studied as interesting matrices for polymer/NP nanohybrids, where NPs synthesized can be selectively incorporated into one of the

a)Electronic addresses: hlchen@che.nthu.edu.tw and hashi2@pearl.ocn.ne.jp

 ©2015 AIP Publishing LLC

This article is copyrighted as indicated in the article. Reuse of AIP content is subject to the terms at: http://scitation.aip.org/termsconditions. Downloaded to IP: 140.110.200.41 On: Fri, 26 Jun 2015 00:57:21

microdomains.[13–20] The NPs confined in one of the selected microdomains have been found to uniformly distribute in the domain space or be localized at the interface between different microdomains or in the middle of the domains.[21,22]

In this work, the metal precursor is deliberately reduced in a homopolymer matrix rather than bcp matrices for exploring the intrinsic interparticle interaction and its consequences on the morphology of NP aggregates without the influence of spatial confinement involved by the bcp microdomains. Here, the metal precursor palladium acetylacetonate ($Pd(acac)_2$) was first mixed homogeneously with a poly(2-vinylpridine) homopolymer (P2VP) and benzyl alcohol which serves as both the reduction agent for the metal salt and solvent for P2VP. The mixture was then heated to the reduction temperature, T_{red}, at which the reduction of the salt occurred to yield Pd atoms which self-assembled (or aggregated) into Pd NPs in the polymer matrix. Using small angle X-ray scattering (SAXS), we will demonstrate that the NPs self-organized to form a hierarchical structure, driven by the hard-core-repulsion and attractive-tail inter-nanoparticle interaction, with three distinct levels, where the primary NPs with the diameter of ~1.8 nm (level one) associated to form local clusters (level two); these clusters then aggregated further to build up a large-scale mass-fractal structure characterized by a fractal dimension of ~2.3 (level three).

II. EXPERIMENTAL SECTION

A. Sample preparation

P2VP with $M_w = 9.1 \times 10^3$ and $M_w/M_n = 1.05$ was purchased from Scientific Polymer Products, Inc., where M_w and M_n are the weight and number average molecular weight, respectively. $Pd(acac)_2$ was acquired from Alfa Aesar. Prescribed amounts of P2VP, benzyl alcohol, and $Pd(acac)_2$ were dissolved in chloroform to obtain a dilute homogeneous solution. Chloroform as one of the solvent was allowed to completely evaporate at room temperature for one day. The resultant mixture, containing P2VP (15.81 wt. %), benzyl alcohol (82.61 wt. %), and $Pd(acac)_2$ (1.58 wt. %), was then heated to $T_{red.}$ to induce the reduction of $Pd(acac)_2$ into Pd NPs for 5 h in a cell used for the SAXS experiment. The sample cell is composed of two Kapton windows which can seal the liquid samples well within the cell to keep the concentration of benzyl alcohol constant during and after the reduction.

B. SAXS measurements

SAXS measurements were performed at Beamline 23A1 at the National Synchrotron Radiation Research Center (NSRRC) located at Hsin-Chu, Taiwan.[23] A two-dimensional Pilatus detector with 981 × 1043 pixels was used to record the SAXS intensity. The energy of the X-ray source and the sample to detector distance were 14 keV and 1876 mm, respectively. The irradiated volume of the sample with the incident beam was cubic, having dimensions 0.5 mm × 0.5 mm normal to the incident beam and 0.5 mm parallel to it (sample thickness). The SAXS intensities obtained were plotted against $q = (4\pi/\lambda)\sin(\theta/2)$, where λ is the wavelength of X-ray ($\lambda = 0.124$ nm) and θ is the scattering angle. The sample to detector distance was calibrated using silver behenate with the primary diffraction peak at 1.076 nm^{-1}. The SAXS profiles were corrected for sample transmission, empty cell transmission, empty cell scattering, detector sensitivity, and the thermal diffuse scattering (TDS) arising from the longitudinal acoustic phonons. The SAXS profiles of all samples, including the nanohybrid films obtained after removing benzyl alcohol, were measured using the same type of sample cell.

C. Transmission electron microscope (TEM) observation

The real-space morphology of the nanohybrid was observed by a JEOL JEM-1230 transmission electron microscope operated at 120 kV. The TEM specimens were prepared by completely evaporating benzyl alcohol from the sample, followed by ultra-microtoming the dried hybrid into ultrathin sections of 50-55 nm in thickness (LEICA ULTRACUT R) at room temperature. Since the SAXS measurements were conducted for the specimens containing benzyl alcohol as described in Sec. II A, effects of evaporating benzyl alcohol on the internal structures of the hybrid were closely investigated by SAXS, as will be detailed below in conjunction with Figure 3.

III. RESULTS

Figure 1 displays the representative TEM micrograph of the hybrid formed at $T_{red.} = 100\,°C$. The micrograph revealed that the Pd NPs were spheres with the number-average diameter of ~4 nm (see the dark dots in the inset). They were not uniformly distributed in the P2VP matrix; instead, they aggregated to form a highly branched superstructure. It is difficult to identify the building block of the superstructure, because the micrograph presents the 2D projection of the real-space structure in three-dimensional (3D) space. Moreover, the micrograph only showed the morphology in a small area of the sample, such that the observed structure may not necessarily represent correctly an ensemble average of the morphology of the whole system. The 3D structure associated with the spatial organization of the NPs statistically averaged over a large area can be best studied by scattering methods, particularly because the large electron density contrast between the metallic NPs and the matrix can yield strong X-ray scattering intensity. Consequently, the morphology of the present hybrid was rigorously and quantitatively characterized by SAXS in this study.

Figure 2 shows the representative SAXS profile of the hybrid, where the metal precursor was reduced at 100 °C for 5 hr to yield Pd NPs distributed in the matrix phase composed of P2VP and benzyl alcohol where the P2VP concentration is ~16 wt. %. Three regions with distinct scattering features as follows were classified in the SAXS profile. At $q > 1$ nm^{-1} (denoted as "Region I"), the intensity profile showed a small peak (marked by "$i = 1$") at q~3 nm^{-1} and a plateau at q~1.5 nm^{-1}. In the intermediate q region (0.2 $nm^{-1} < q < 0.9$ nm^{-1}; denoted as "Region II"), a broad hump (marked by the arrow) was identified at q~0.4 nm^{-1}. At $q < 0.2$ nm^{-1},

This article is copyrighted as indicated in the article. Reuse of AIP content is subject to the terms at: http://scitation.aip.org/termsconditions. Downloaded to IP: 140.110.200.41 On: Fri, 26 Jun 2015 00:57:21

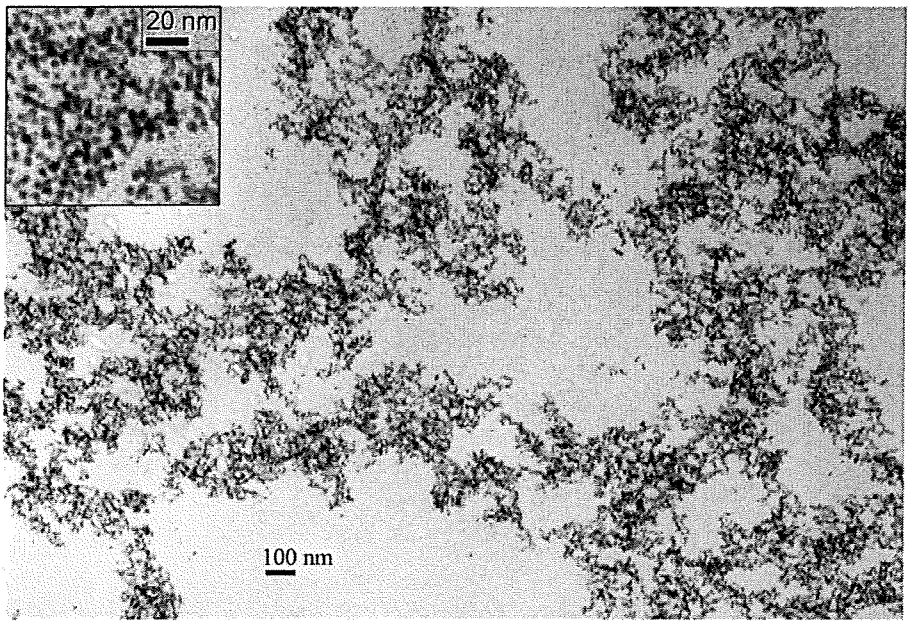

FIG. 1. A representative TEM micrograph showing the formation of a branched superstructure of the Pd NPs in P2VP matrix ($T_{red.}$: 100 °C). The inset displays the enlarged micrograph.

the intensity exhibited an upturn with decreasing q, compared with the intensity distribution in Region II, and this region was denoted as "Region III."

The branched superstructure formed by the Pd NPs revealed by the TEM micrograph in Figure 1 may provide a useful guideline for choosing the plausible model for analyzing the SAXS profile. However, it should be noted that the SAXS sample giving rise to Figure 2 contained benzyl alcohol (by ~82.6 wt. %), while the TEM thin section did not; thus, it is necessary to examine whether or not the NP organization in the hybrid was conserved after removal of benzyl alcohol.

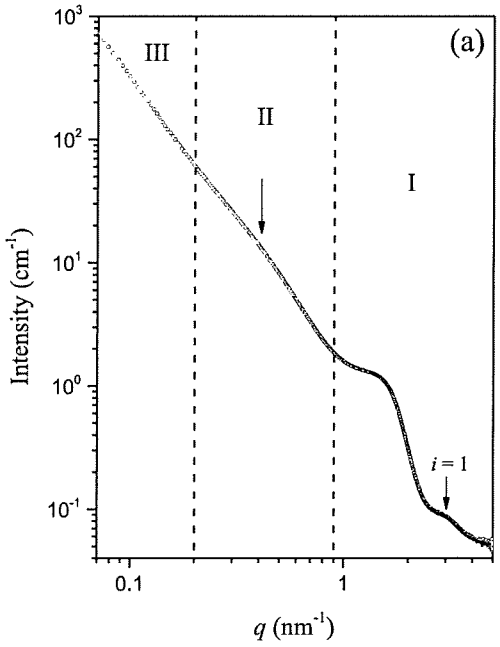

FIG. 2. The representative SAXS profile of the hybrid observed over the entire accessible q range. The hybrid was prepared by reducing $Pd(acac)_2$ in the P2VP solution in benzyl alcohol at 100 °C for 5 h.

Figure 3 shows the SAXS profiles of the hybrid before [profile (1)] and after [profile (2)] evaporating benzyl alcohol. It was found that the two SAXS profiles completely overlapped each other by a vertical shift in the double logarithmic plot, which demonstrates that the spatial distribution of NPs was retained even after removing benzyl alcohol, at least over the

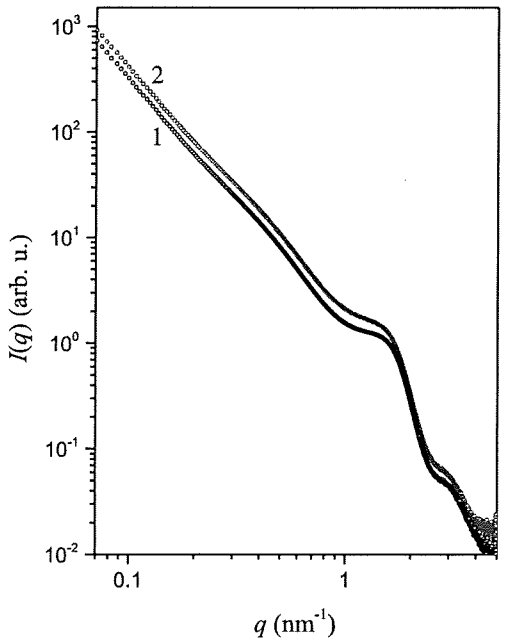

FIG. 3. The representative SAXS profiles of the hybrid prepared by reducing $Pd(acac)_2$ in the P2VP solution with benzyl alcohol at 100 °C for 5 h. Profile (1) and profile (2) represent the SAXS profile of the sample before and after removing benzyl alcohol, respectively, both profiles being corrected for the TDS. Profile (2) displayed in the figure was vertically shifted in the double logarithmic plot, partly because the vertical shift facilitates comparisons of the intensity distribution with respect to q for the profiles (1) and (2), and partly because the film obtained after removal of benzyl alcohol was not uniform in thickness for the accurate conversion of the measured intensity into the absolute intensity scale of cm^{-1}. However, profile (1) was not vertically shifted, so that it was presented as the absolute intensity scale of cm^{-1}.

This article is copyrighted as indicated in the article. Reuse of AIP content is subject to the terms at: http://scitation.aip.org/termsconditions. Downloaded to IP: 140.110.200.41 On: Fri, 26 Jun 2015 00:57:21

length scale $l(= 2\pi/q \leqq 90$ nm) covered by the present SAXS experiment. Therefore, the TEM micrograph obtained with the specimens after the removal of benzyl alcohol can reflect the real morphology of the hybrid with the presence of benzyl alcohol, at least over $l \leqq 90$ nm. This evidence itself revealed that the percolated structure of the NPs formed in the polymer solution was sufficiently strong to be retained after the solvent removal.

The TEM micrograph along with the identification of three distinct q regions in the SAXS profile strongly suggests that the system formed a hierarchical structure with three levels characterized by the characteristic scattering features in the corresponding q regions. The scattering behavior of the hierarchical structure with arbitrary number of levels has been described by the Beaucage model.[24] This model assumes that the scattering intensity distribution of each structural level is expressed by a combination of the Guinier's scattering functions[25] characterized by the radii of gyration of the upper and lower cutoff structure units (respectively, defined by $R_{g,U}$ and $R_{g,L}$) and a structurally limited power law scattering function characterized by the power law together with the upper and lower damping functions (respectively, defined by D_U and D_L). Here, $R_{g,U}$ and $R_{g,L}$ correspond to the upper and lower cutoff sizes of the structural units, respectively, and D_U and D_L are characterized also by $R_{g,U}$ and $R_{g,L}$, respectively. In this case, the exponent of the power law reflects the characteristic fractal dimension of the morphological entity associated with the given structural level. The Beaucage model has been adopted successfully to resolve the hierarchical structures of various systems, e.g. carbon black NPs dispersed in rubber-like polymer matrices.[26] This model may be able to phenomenologically describe the scattering features of the present hybrid also, although the phenomenological model has the following drawbacks. (1) It does not explicitly account for the nature of interparticle interactions which is the most important basic physical factor leading to the observed hierarchical structure. (2) It does not clearly predict the physical origin of the structural units characterized by $R_{g,U}$ and $R_{g,L}$, and the values $R_{g,U}$ and $R_{g,L}$ themselves are more or less affected in practice by the interparticle interference effect on the scattering waves from the upper cutoff structural units and by that from the lower cutoff structural units, respectively. Thus, here we develop a new hierarchical structure model that provides an adequate description of the observed scattering profile over the entire q range with a particular aim to clarify the nature of the physical interactions between the NPs and the physical origin of the structural units. The formulation of the structural model and the relevant theoretical background are elaborated in Sec. IV.

IV. THEORETICAL BACKGROUND

The hierarchical structure model developed here is composed of three levels. Level one corresponds to the Pd spherical NPs generated by the reduction of salt, and it contributes predominantly to the scattering intensity in Region I. The small peak marked by "$i = 1$" in Region I (see Figure 2) was hence attributed to the first-order form factor maximum of the primary NPs. The NPs may interact through a relevant interparticle interaction which suppressed the intensity in the plateau near 1.5 nm^{-1} from that described by the Guinier's law predicted for the independent spherical NPs (as will be demonstrated later in Figure 5).

The scattering profile in Region II showed a broad hump which resembles a form factor profile of a higher-order structure of the NPs in the q range close to its Guinier region. We attributed this structural entity to the cluster formed by the association of a number of NPs (level two) and the characteristic form factor of this kind of cluster contributed to the intensity in Region II and the hump.

The intensity upturn with decreasing q was observed in Region III located in the low-q region. This q-dependence of the intensity is described by the power law associated with a fractal object denoted by $I(q) \sim q^{-D_m}$ with D_m being the mass fractal dimension. Hence, we postulated that the clusters themselves further self-assembled into a large-scale mass-fractal structure (level three) with the mass fractal dimension of D_m.

To formulate the scattering function associated with the proposed hierarchical structure, we will start with introducing the scattering functions of interacting spherical NPs distributed in an infinitely large space. This condition is fulfilled when the clusters are not formed in the system. Then, we proceed to formulate the scattering from a cluster formed by the assembly of a number of NPs by limiting the space over which the interacting particles are distributed. Finally, we will incorporate the mass-fractal structure factor for a spatial distribution of centers of mass of the clusters to predict the whole scattering function of the hierarchical structure that well fits with the experimentally observed SAXS profiles of the hybrids.

A. Scattering from the interacting spherical particles distributed over an infinitely large space

The differential scattering cross section $d\Sigma(q)/d\Omega$ from a collection of primary spherical NPs distributed over an infinitely large medium, which is usually characterized by the irradiated volume V_{ir} with the incident beam, is generally given by the Zernike-Prins (ZP) equation,[27]

$$\frac{d\Sigma(q)}{d\Omega} = P(q)S(q), \tag{1}$$

where $P(q)$ is the form factor of the spheres which are assumed here to be monodisperse in size, $S(q)$ is the ZP structure factor given by

$$S(q) = N_t\left[1 + n\int_0^\infty g(r)\frac{\sin qr}{qr}4\pi r^2 dr\right], \tag{2}$$

where N_t is the total number of the spheres in the infinitely large space, $n = N_t/V_{ir}$, and $g(r)$ is the radial distribution function of the particles in the liquids. Substituting $g(r)$ by $[g(r) - 1] + 1$ and noting that

$$g(r) - 1 = h(r), \tag{3}$$

This article is copyrighted as indicated in the article. Reuse of AIP content is subject to the terms at: http://scitation.aip.org/termsconditions. Downloaded to IP: 140.110.200.41 On: Fri, 26 Jun 2015 00:57:21

where $h(r)$ is the total correlation function,[28] the integral in Eq. (2) is rewritten as

$$\int_0^\infty g(r)\frac{\sin qr}{qr}4\pi r^2 dr = T(q) + \int_0^\infty h(r)\frac{\sin qr}{qr}4\pi r^2 dr, \tag{4}$$

where

$$T(q) \equiv \int_0^\infty \frac{\sin qr}{qr}4\pi r^2 dr = \int_{\mathcal{V}_{ir}} \frac{\sin qr}{qr}4\pi r^2 dr \tag{5a}$$

$$= \pi^3\delta(q). \tag{5b}$$

The term $T(q)$ in Eq. (5a) is the Fourier transform of the homogeneous space extending over the infinite space which is practically equal to the volume V_{ir} irradiated by the incident beam: Thus, $T(q)$ involves the volume integral over the irradiated volume V_{ir} as shown in the second line of Eq. (5a). This volume is large enough so that $T(q)$ is given by $\delta(q)$, Dirac's delta function, times π^3 for a rectangular parallepiped irradiated volume as given by Eq. (5b) (see the Appendix for the reason why π^3 should be multiplied). Thus,

$$S(q) = N_t[\pi^3 n\delta(q) + S_{ZP}(q)], \tag{6}$$

with S_{ZP} defined by

$$S_{ZP}(q) = 1 + n\int_0^\infty h(r)\frac{\sin qr}{qr}4\pi r^2 dr = 1 + nh(q), \tag{7}$$

where $h(q)$ is the Fourier transform of $h(r)$ defined later by Eq. (11). Since $S(q)$ is usually discussed in the q range at $q > 0$, excluding the case of $q = 0$, the first term $\pi^3 n\delta(q)$ in Eq. (6) is usually dropped out. However, this term becomes important in the case where the interacting particles are confined in the cluster of a finite size, as will be detailed later in Sec. IV B.

The total correlation function $h(r)$ can be expressed in terms of the direct correlation function $C(r)$ via the Ornstein-Zernike (OZ) equation[28] given below,

$$h(r) = C(r) + nC(r) * h(r), \tag{8}$$

where the asterisk "*" denotes the convolution operation in 3D space generally defined below by Eq. (9), even though $C(r)$ and $h(r)$ are spherically symmetric functions which depend only on r,

$$C(\mathbf{r}) * h(\mathbf{r}) = \int C(\mathbf{u})\, h(\mathbf{r}-\mathbf{u})\, d\mathbf{u} = \int h(\mathbf{u})\, C(\mathbf{r}-\mathbf{u})\, d\mathbf{u}, \tag{9}$$

where $\mathbf{r}$ and $\mathbf{u}$ are the vectors in the 3D real space, and $\int d\mathbf{u}$ designates a volume integral in the 3D real space.

Fourier transform of Eq. (8) gives

$$h(q) = C(q) + nC(q)\, h(q), \tag{10}$$

where

$$X(q) \equiv \int_0^\infty X(r)\frac{\sin qr}{qr}4\pi r^2 dr, \tag{11}$$

with

$$X(r) = h(r) \text{ or } C(r).$$

Substituting Eq. (10) into Eq. (7) leads to

$$S_{ZP}(q) = \frac{1}{1 - nC(q)}. \tag{12}$$

The structure factor $S_{ZP}(q)$ depends directly on $C(q)$. Thus, $S_{ZP}(q)$ can be obtained, if $C(q)$ can be calculated. The relationships among $C(r)$, $g(r)$, and the potential energy for the interparticle interaction $u(r)$, i.e., the so-called Hypernetted Chain (HPC) equation and Percus-Yevick (PY) equation,[29] were calculated by the cluster expansion of the two-particle distribution function.[30] It is noted that the two equations of HPC and PY are different with respect to the approximations involved in calculating the cluster integrals. Below, we shall consider the scattering theory based on the PY equation[29] given by

$$C(r) = g(r)\{1 - \exp[u(r)/k_B T]\} \tag{13}$$

applied for spherical particles having hard-core repulsion as well as for those having the hard-core repulsion and an attractive tail potential.[31,32]

1. The hard-core potential with the PY closure (hard-sphere model (HS model))

Wertheim[33] solved the analytical solution for $C(r)$, denoted hereafter by $C_{HS}(r)$, for spheres having the hard-core repulsive potential $u(r)$ given by Eq. (14) below (see also Figure 4(a)) on the basis of the PY closure given by Eq. (13),

$$u(r) = \begin{cases} +\infty, & \text{for } r < 2R_P \\ 0, & \text{for } r \geq 2R_P \end{cases}, \tag{14}$$

where R_p is the radius of the sphere. We denote hereafter the spheres which obey those characteristics as described above as the HS model. The result for $C_{HS}(r)$ is given by

$$C_{HS}(r) = \begin{cases} -(\alpha + \beta s + \gamma s^3)/(1-\phi)^4, & \text{for } s \leq 1 \\ 0, & \text{for } s > 1 \end{cases}, \tag{15}$$

where s and ϕ are the reduced distance and the volume fraction of the spheres in the system, respectively, given by

$$s \equiv r/(2R_p), \quad \phi \equiv (4\pi {R_p}^3/3)n. \tag{16}$$

Thus, $C(q)$ in Eq. (10), denoted hereafter as $C_{HS}(q)$, is given by the Fourier transform of $C_{HS}(r)$ (see Eq. (11) with a replacement of X by C_{HS}). Here, the coefficients α, β, and γ in Eq. (15) depend on ϕ, as given by

$$\begin{aligned} \alpha &= (1 + 2\phi)^2, \\ \beta &= -6\phi[(1 + (\phi/2))]^2, \\ \gamma &= (1/2)\,\phi(1 + 2\phi)^2. \end{aligned} \tag{17}$$

$C_{HS}(q)$ is readily evaluated[34] to give the structure factor $S_{ZP}(q)$ given by Eq. (12), which is denoted hereafter as $S_{HS/inf}(q)$,

$$S_{HS/inf}(q) = [1 - nC_{HS}(q)]^{-1} = \{1 + 24\phi[G(A)/A]\}^{-1}, \tag{18}$$

where

This article is copyrighted as indicated in the article. Reuse of AIP content is subject to the terms at: http://scitation.aip.org/termsconditions. Downloaded to IP: 140.110.200.41 On: Fri, 26 Jun 2015 00:57:21

$$A = 2qR_p,$$
$$G(A) = \frac{\alpha}{A^2}(\sin A - A\cos A) + \frac{\beta}{A^3}[2A\sin A + (2 - A^2)\cos A - 2] + \frac{\gamma}{A^5}\{-A^4\cos A + 4[(3A^2 - 6)\cos A + (A^3 - 6A)\sin A + 6]\}. \quad (19)$$

2. The sticky-hard-sphere potential with the PY closure (SHS model)

Baxter solved the PY closure analytically in the case where $u(r)$ consists of a hard-core repulsion with a rectangular attractive well in the limit in which the range of the well becomes zero and its depth is infinite.[31,32] This SHS model of Baxter can account for the first-order phase transition that cannot be accounted for by the HS model of qualitatively the same type as that observed numerically for the Lennard-Jones potential[35] which is more realistic than the potential used for the SHS model. Menon *et al.*[36] derived an analytical solution for a modified SHS model with a more realistic potential $u(r)$ with a finite width Δ and a finite depth $u_0 < 0$, as given by Eq. (21) below and as schematically illustrated in Figure 4(b), on the basis of a perturbation theory with the parameter ε defined by

$$\varepsilon \equiv \Delta/(2R_p + \Delta), \quad (20)$$

in the case where ε is smaller than 0.1,

$$u(r) = \begin{cases} \infty, & \text{for } r \le 2R_p \\ u_0, & \text{for } 2R_p \le r \le 2R_p + \Delta \\ 0, & \text{for } 2R_p + \Delta \le r \end{cases}. \quad (21)$$

They utilized the Wiener-Hopf factorization of the OZ equation (Eq. (8)), which was introduced by Baxter[32] and the PY closure (Eq. (13)). The depth of the attractive well $u_0 < 0$ and the perturbation parameter ε define the dimensionless parameter called "stickiness" (τ),

$$\tau = \frac{1}{12\varepsilon}\exp(u_0/k_BT). \quad (22)$$

The corresponding structure factor $S_{ZP}(q)$ in Eq. (12), denoted hereafter as $S_{SHS/inf.}(q)$, of the sticky hard spheres with the potential $u(r)$ given by Eq. (21) dispersed in an infinitely large space is also given analytically. We use the following analytical formulas for $S_{SHS/inf.}(q)$ presented by Baxter[31] and Menon *et al.*:[36]

$$S_{SHS/inf.}(q) = [A^2(q) + B^2(q)]^{-1}, \quad (23)$$

where

$$A(q) = 1 + 12\eta\left\{\alpha_1\frac{\sin u_a - u_a\cos u_a}{u_a^3} + \beta_1\frac{1 - \cos u_a}{u_a^2} - \frac{\lambda}{12}\frac{\sin u_a}{u_a}\right\}, \quad (24)$$

$$B(q) = 12\eta\left\{\alpha_1\left[\frac{1}{2u_a} - \frac{\sin u_a}{u_a^2} + \frac{1 - \cos u_a}{u_a^3}\right] + \beta_1\left[\frac{1}{u_a} - \frac{\sin u_a}{u_a^2}\right] - \frac{\lambda}{12}\frac{1 - \cos u_a}{u_a}\right\}. \quad (25)$$

$u_a = qa$, $a = 2R_p + \Delta$, η is the effective volume fraction of the spheres having the radius $a/2(= R_p + \Delta/2)$ as given by

$$\eta = \frac{\pi a^3}{6}n = \left(\frac{a}{2R_p}\right)^3\phi \quad (26)$$

and

$$\alpha_1 = \frac{1 + 2\eta - \mu}{(1 - \eta)^2}, \quad \beta_1 = \frac{(-3\eta + \mu)}{2(1 - \eta)^2}, \quad \mu = \lambda\eta(1 - \eta). \quad (27)$$

The parameter λ is a solution of the quadratic equation given by

$$\frac{\eta}{12}\lambda^2 - \left(\tau + \frac{\eta}{1 - \eta}\right)\lambda + \frac{1 + (\eta/2)}{(1 - \eta)^2} = 0. \quad (28)$$

B. Scattering from the cluster composed of the primary particles: Effect of spatial confinement of the particles

Hashimoto *et al.*[37] have characterized the NPs encapsulated within the aggregate of the dendrimer molecules (designated as "template") by a combination of small-angle neutron scattering (SANS) and SAXS. In this case, the NPs were distributed over a confined space designated as the template instead of an infinitely extended space as in the HS or SHS model described above. Below, we specifically rewrite

This article is copyrighted as indicated in the article. Reuse of AIP content is subject to the terms at: http://scitation.aip.org/termsconditions. Downloaded to IP: 140.110.200.41 On: Fri, 26 Jun 2015 00:57:21

the scattering from the HS and the SHS confined in the cluster on the basis of the same scheme as that in Ref. 37.

The electron density distribution for the assembly of the spheres in the cluster $\rho_c(\mathbf{r})$ is expressed in terms of the spatial distribution of the centers of the spheres $\rho_{\text{center,c}}(\mathbf{r})$ in the cluster and the electron density distribution of the spheres around their centers $\rho_p(\mathbf{r})$ by

$$\rho_c(\mathbf{r}) = \rho_{\text{center,c}}(\mathbf{r}) * \rho_p(\mathbf{r}), \tag{29}$$

where "$*$" designates the convolution operation defined by Eq. (9). $\rho_{\text{center,c}}(\mathbf{r})$ in turn is expressed with respect to the shape factor of the cluster $\sigma(\mathbf{r})$ and the spatial distribution of the spheres spread over infinite space $\rho_{\text{center},\infty}(\mathbf{r})$ under a concept that $\rho_{\text{center},\infty}(\mathbf{r})$ has the same statistical characteristic as $\rho_{\text{center,c}}(\mathbf{r})$: As a direct consequence of this concept, we have such a condition that $n = N_t/V_{ir} = N_c/V_c$ where N_c and V_c are the number of NPs in the cluster and the volume of the cluster, respectively. Consequently,

$$\rho_{\text{center,c}}(\mathbf{r}) = \rho_{\text{center},\infty}(\mathbf{r})\sigma(\mathbf{r}), \tag{30}$$

where

$$\sigma(r) = \begin{cases} 1, & \text{if } \boldsymbol{r} \in \text{cluster} \\ 0, & \text{if } \boldsymbol{r} \notin \text{cluster} \end{cases}. \tag{31}$$

The differential scattering cross section from a cluster of the particles $d\Sigma(\mathbf{q})/d\Omega$ is given by

$$\frac{d\Sigma(\mathbf{q})}{d\Omega} = \int \tilde{\tilde{\rho}}_c(\mathbf{r}) \exp(-i\mathbf{q}\cdot\mathbf{r})\, d\mathbf{r} \equiv \tilde{\tilde{\rho}}_c(\mathbf{q}), \tag{32}$$

where $\tilde{\tilde{\rho}}_c(\mathbf{r})$ is the autocorrelation function or the convolution square of $\rho_c(\mathbf{r})$ defined by

$$\tilde{\tilde{\rho}}_c(\mathbf{r}) = \int d\mathbf{r}_1 \rho_c(\mathbf{r}_1)\rho_c(\mathbf{r}_1 + \boldsymbol{r}) \tag{33}$$

and $\tilde{\tilde{\rho}}_c(\mathbf{q})$ is the Fourier transform of $\tilde{\tilde{\rho}}_c(\mathbf{r})$. From Eq. (29),

$$\tilde{\tilde{\rho}}_c(\mathbf{r}) = \tilde{\tilde{\rho}}_{\text{center,c}}(\mathbf{r}) * \tilde{\tilde{\rho}}_p(\mathbf{r}), \text{ using Eq. (30)}$$

$$\tilde{\tilde{\rho}}_c(\mathbf{r}) = \frac{1}{V_{ir}}[\tilde{\tilde{\rho}}_{\text{center},\infty}(\mathbf{r})\,\tilde{\tilde{\sigma}}(\mathbf{r})] * \tilde{\tilde{\rho}}_p(\mathbf{r}). \tag{34}$$

Taking Fourier transform of Eq. (34),

$$\frac{d\Sigma(q)}{d\Omega} = \tilde{\tilde{\rho}}_c(\mathbf{q}) = \frac{1}{V_{ir}}[\tilde{\tilde{\rho}}_{\text{center},\infty}(\mathbf{q}) * \tilde{\tilde{\sigma}}(\mathbf{q})]\,\tilde{\tilde{\rho}}_p(\mathbf{q}). \tag{35}$$

For spherically symmetric systems as in our case, $\mathbf{q}$ is replaced by its scalar quantity q. $\tilde{\tilde{\rho}}_{\text{center},\infty}(q)$ is equal to $S(q)$ given by the ZP equation (Eq. (6)) and $\tilde{\tilde{\rho}}_p(q)$ is given by the form factor of the single particle $P(q)$. Thus, Eq. (35) is rewritten by

$$\frac{d\Sigma(q)}{d\Omega} = \frac{1}{V_{ir}} P(q)\left[S(q) * \tilde{\tilde{\sigma}}(q)\right]. \tag{36}$$

Again, the symbol $*$ denotes the 3D convolution operation in q space. From Eqs. (6) and (36) and noting that $\delta(q) * \tilde{\tilde{\sigma}}(q) = \tilde{\tilde{\sigma}}(q)$ and $N_t/V_{ir} = n$, we obtain

$$\frac{d\Sigma(q)}{d\Omega} = nP(q)[\pi^3 n\,\tilde{\tilde{\sigma}}(q) + S_{ZP}(q) * \tilde{\tilde{\sigma}}(q)]. \tag{37}$$

The first term in the parenthesis [ ] at the right hand side (rhs) of Eq. (37) physically implies a contribution of the scattering from the homogeneous single cluster having the average number density of the particles n, which controls the average contrast of the cluster against its surrounding medium, to the net scattering. On the other hand, the second term in the parenthesis at the rhs of Eq. (37) indicates a contribution of the scattering from the fine structure within the cluster, which reflects the spatial distribution of the particles within the cluster, to the net scattering.

In the case when the particle and the cluster are the spheres of radius R_p and R_c, respectively,

$$P(q) = \Delta\rho^2 V_p^2 \Phi^2(u_p), \quad u_p = qR_p, V_p = 4\pi {R_p}^3/3, \tag{38}$$

where $\Delta\rho$ is the electron density difference between NPs and the matrix phase,

$$\tilde{\tilde{\sigma}}(q) = V_c^2 \Phi^2(u_c), \quad u_c = qR_c, \quad V_c = 4\pi R_c^3/3, \tag{39}$$

where

$$\Phi(u) = \frac{3}{u^3}(\sin u - u\cos u). \tag{40}$$

From Eqs. (37) to (39),

$$\frac{d\Sigma(q)}{d\Omega} = n\Delta\rho^2 V_p^2 V_c^2 \Phi^2(u_p)[\pi^3 n\Phi^2(u_c) + S_{ZP}(q) * \Phi^2(u_c)]. \tag{41}$$

C. Effect of polydispersity in cluster size and particle size

So far, we have assumed that the size of the cluster and that of the particle are monodisperse. Let us now consider the effect of the polydispersity on $d\Sigma(q)/d\Omega$ in Eq. (41). In the

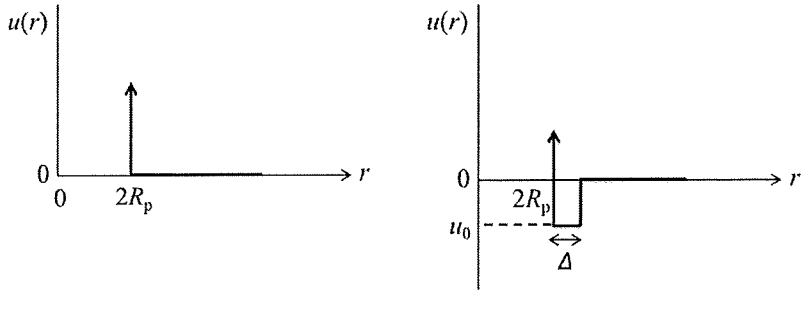

FIG. 4. Schematic representations of the potential energy of spheres $u(r)$ having (a) hard-core repulsion and (b) hard-core repulsion and attractive potential well.[36]

This article is copyrighted as indicated in the article. Reuse of AIP content is subject to the terms at: http://scitation.aip.org/termsconditions. Downloaded to IP: 140.110.200.41 On: Fri, 26 Jun 2015 00:57:21

case when the polydispersity exists, Eq. (41) is rewritten by

$$\frac{d\Sigma(q)}{d\Omega} = K\{\pi^3 n\langle V_p^2\Phi^2(q;R_p)\,V_c^2\Phi^2(q;R_c)\rangle + \langle V_p^2\Phi^2(q;R_p)\,[S_{ZP}(q;R_p) * V_c^2\Phi^2(q;R_c)]\rangle\}, \quad (42)$$

where $K \equiv n\Delta\rho^2$ and $\langle\ \ \rangle$ denotes averages with respect to the distribution of R_p and R_c. The ZP structure factor $S_{ZP}(q;R_p)$ depends on the size distribution of R_p through the radial distribution function $g(r)$ of the particles.

In calculating S_{ZP}, one must take into account the fact that all the pairs i, j of spheres having the size R_{pi} and $R_{pj}(i.j = 1,\cdots,m)$ affect $g(r)$. Here, m is the number of the components having different R_p's, and $n = \sum_{i=1}^{i=m} n_i$ where n_i is the number density of ith sphere having the radius R_{pi}. Thus, the calculation of $g(r)$ and $S_{zp}(q;R_{pi})$ $(i = 1,\cdots,m)$ for the polydisperse particles is quite complex. In order to simplify the complex problem, we adopt here the so-called "average structure factor approximation"[38] where $S_{ZP}(q;R_{pi})$ $(i = 1,\cdots,m)$ for the polydisperse spheres is assumed to be equal to $S_{ZP}(q;R_{p,av})$, the ZP structure factor for the monodisperse sphere having the average size $R_{p,av}$ (assumption 1). We also adopt the approximation of "independence between the size distribution of the cluster and that of the spherical particle" (assumption 2). In the context of assumption 2,
[The 1st term of rhs of Eq. (42)]

$$= K\pi^3 n\left\langle V_p^2\Phi^2(q;R_p)\right\rangle\left\langle V_c^2\Phi^2(q;R_c)\right\rangle. \quad (43)$$

In the context of assumptions 1 and 2,
[The 2nd term of rhs of Eq. (42)]

$$= K\left\langle V_p^2\Phi^2(q;R_p)\right\rangle[S_{ZP}(q;R_{p,av}) * \langle V_c^2\Phi^2(q;R_c)\rangle]. \quad (44)$$

Each average $\langle\ \ \rangle$ is given by

$$\langle V_k^2\Phi^2(q;R_k)\rangle = \int_0^\infty P_N(R_k)\left(\frac{4\pi}{3}R_k^3\right)^2\Phi^2(q;R_k)\,dR_k, \text{ with } k = \text{p or c}, \quad (45)$$

where $P_N(R_k)$ is the normalized distribution function for the number of the NPs having the radius $R_k(k = p)$ or that of the cluster having the radius $R_c(k = c)$,

$$R_{p,av}^3 \equiv \int_0^\infty P_N(R_p)R_p^3 dR_p. \quad (46)$$

Equations (42) and (46) imply that the number density of the spheres and the total volume fraction of spheres are independent of its size distribution. We assume that $P_N(R_p)$ is given by the Schulz distribution[39]

$$P_N(R_k) = (Z+1)^{Z+1}X^Z\left\{\frac{\exp[-(Z+1)X]}{\langle R_k\rangle\Gamma(Z+1)}\right\} \text{ with } k = \text{p or c}. \quad (47)$$

Here, $X \equiv R_k/\langle R_k\rangle$, where $\langle R_k\rangle$ is the number-average radius of the k spices, $Z = (1/P_k^2) - 1$ is related to the polydispersity of k, $P_k = \sigma_k/\langle R_k\rangle$ with ${\sigma_k}^2$ being the variance of the distribution, and $\Gamma(Z)$ is the gamma function.

Consequently, the scattering from the polydisperse cluster and particles is given by Eqs. (42)–(47) where $S_{ZP}(q;R_{p,av})$ is replaced by $S_{HS/inf.}(q;R_{p,av})$ for the HS in the cluster which is given by Eqs. (17)–(19) with a replacement of R_p by $R_{p,av}$ or by $S_{SHS/inf.}(q;R_{p,av})$ for the SHS in the cluster which is given by Eqs. (23)–(28) with a replacement of a by $a_{av} = 2R_{p,av} + \Delta$.

D. Scattering from the mass-fractal structure built up by the clusters of NPs

Here, we investigate whether the intensity upturn with decreasing q observed in Region III of the SAXS profile was attributed to the formation of a mass-fractal structure built up by the clusters of Pd NPs. The net scattering intensity distribution $d\Sigma_{net}(q)/d\Omega$ from the mass-fractal structure thus formed is given by

$$d\Sigma_{net}(q)/d\Omega = [d\Sigma_{MF}(q)/d\Omega][d\Sigma_{cluster}(q)/d\Omega], \quad (48)$$

where $d\Sigma_{cluster}(q)/d\Omega$ is given by Eq. (42), and $d\Sigma_{MF}(q)/d\Omega$ is the scattering profile from the spatial distribution of centers of mass of the clusters characterized by the mass-fractal structure,

$$d\Sigma_{MF}(q)/d\Omega = CS_{MF}(q), \quad (49)$$

with C being the proportionality constant and the structure factor $S_{MF}(q)$ is given by[40]

$$S_{MF}(q) = 1 + \frac{D_m\Gamma(D_m-1)\sin[(D_m-1)\tan^{-1}(q\xi)]}{(qR_{c,f})^{D_m}[1+(q\xi)^{-2}]^{(D_m-1)/2}}, \quad (50)$$

where D_m is the mass-fractal dimension; $\Gamma(x)$ is the gamma function of argument x; ξ is the upper cut-off length that characterizes the size of the upper bound of the mass-fractal object in real space, $R_{c,f}$ is the lower cut-off length of the mass-fractal object that should satisfy $R_{c,f} \geqq 2R_c$.$S_{MF}(q)$ given by Eq. (50) has the following asymptotic behaviors:

$$S_{MF}(q) \propto \begin{cases} q^{-D_m}, & \text{when } q_\xi < q < q_{R_{c,f}} \\ 1, & \text{when } q > q_{R_{c,f}} \end{cases}, \quad (51)$$

where $q_{Rc,f} = 2\pi/R_{c,f}$, and $q_\xi = 2\pi/\xi : q_\xi$ and $q_{Rc,f}$ are the upper and lower cut-off wave numbers of the mass fractal object. Thus, $d\Sigma_{net}(q)/d\Omega$ has the following asymptotic behaviors:

$$d\Sigma_{net}(q)/d\Omega = \begin{cases} (\text{constant})q^{-D_m}d\Sigma_{cluster}(q)/d\Omega, & \text{when } q_\xi < q < q_{R_{c,f}} \\ d\Sigma_{cluster}(q)/d\Omega, & \text{when } q > q_{R_{c,f}} \end{cases} \quad (52)$$

V. ANALYSIS

Now we apply the scattering functions developed above to analyze the experimentally observed SAXS profile shown in Figure 2. First, we analyze the intensity profile in Regions I and II using Eqs. (42)–(47) to verify the formation of clusters by the NPs and to clarify the nature of the interaction between the particles confined within the clusters. After identifying the appropriate interaction potential of the NPs, we then fit the entire scattering profile using Eqs. (48) and (50) which incorporated the scattering from the mass-fractal structure built up by the clusters composed of the interacting NPs.

This article is copyrighted as indicated in the article. Reuse of AIP content is subject to the terms at: http://scitation.aip.org/termsconditions. Downloaded to IP: 140.110.200.41 On: Fri, 26 Jun 2015 00:57:21

A. Analysis based on the clusters composed of HS

First, we assumed that the NPs confined within the clusters experienced the interparticle interaction with the excluded volume effect in the context of the PY model. According to Eqs. (42)–(44), the scattering intensity from the clusters is expressed as

$$I_{\mathrm{HS/cluster}}(q) = K_2\{\pi^3 n \left\langle V_{\mathrm{p}}^2\Phi^2(q;R_{\mathrm{p}})\right\rangle \left\langle V_{\mathrm{c}}^2\Phi^2(q;R_{\mathrm{c}})\right\rangle + \left\langle V_{\mathrm{p}}^2\Phi^2(q;R_{\mathrm{p}})\right\rangle [S_{\mathrm{HS/inf}}(q;R_{\mathrm{p,av}}) * \left\langle V_{\mathrm{c}}^2\Phi^2(q;R_{\mathrm{c}})\right\rangle]\}. \quad (53)$$

Note that $S_{\mathrm{ZP}}(q;R_{\mathrm{p,av}})$ in Eq. (44) is given by $S_{\mathrm{HS/inf.}}(q;R_{\mathrm{p,av}})$ in this case.

Here, $K_2 = K_1K$, because the scattering intensity $I(q)$ is related to $\mathrm{d}\Sigma(q)/\mathrm{d}\Omega$ by $I(q) = K_1\mathrm{d}\Sigma(q)/\mathrm{d}\Omega$, where $K_1 = I_0/R_{\mathrm{D}}^2$ with I_0 and R_{D} being the incident beam intensity and the distance between the detector and the sample, respectively. Using Eq. (53) and the equations of the average form factor of the polydisperse sphere for the cluster and the NPs, $\langle V_k^2\Phi^2(q;R_k)\rangle$ (k = p or c), the scattering profile of $I_{\mathrm{HS/cluster}}(q)$ was calculated for a set of the parameters: $\langle R_{\mathrm{c}}\rangle = 4.2$ nm with the polydispersity $P_{\mathrm{c}} = 0.01$, $\langle R_{\mathrm{p}}\rangle = 1.8$ nm with the polydispersity $P_{\mathrm{p}} = 0.16$, as shown by profile (4) in Figure 5. The intensity of the polydisperse sphere form factor, $I_{\mathrm{INP}}(q) = K_2\langle V_{\mathrm{p}}^2\Phi^2(q;R_{\mathrm{p}})\rangle$ [the red profile (2)], and the intensity profile associated with the PY hard spheres dispersed over an infinitely large medium $I_{\mathrm{HS/inf.}}(q) = K_2\left\langle V_{\mathrm{p}}^2\Phi^2(q;R_{\mathrm{p}})\right\rangle S_{\mathrm{HS/inf.}}(q;R_{\mathrm{p,av}})$ [the blue profile (3)] were also calculated and displayed in the figure to demonstrate the necessity of incorporating interparticle interaction and cluster formation in the model.

The calculated polydisperse sphere form factor, i.e., $I_{\mathrm{INP}}(q)$ or profile (2), agreed very well with the experimental profile (1) marked by $I_{\mathrm{exp}}(q)$ at $q > 1.7$ nm^{-1}, hence allowing a straightforward and precise determination of $\langle R_{\mathrm{p}}\rangle$ and P_{p} as described above. The agreement also confirms that the small peak marked by "$i = 1$" in Figure 2 corresponds to the first-order maximum of the sphere form factor. The average diameter (~3.6 nm) of the NP determined from the form factor fitting agreed well with that deduced from the TEM micrograph in Figure 1. An obvious difference between the calculated profile and the observed one was found at $q < 1.7$ nm^{-1}, where the observed intensity at a relatively large q region of 0.5 nm^{-1} < q < 1.7 nm^{-1} was lower than that predicted by the Guinier's law predicted from the calculated form factor $I_{\mathrm{INP}}(q)$. This suppression of the scattering intensity is a clear indication of a significant effect of interparticle interference effects on the scattered X-ray.

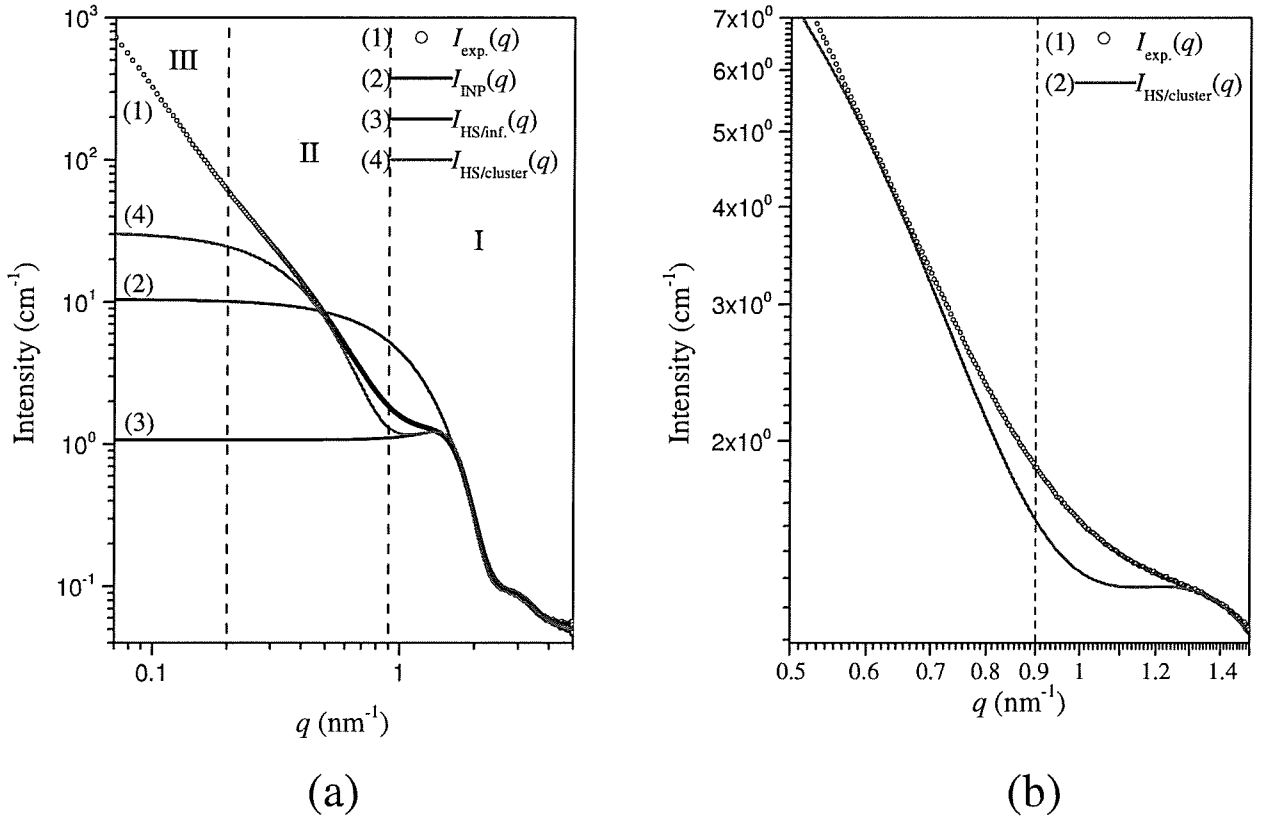

FIG. 5. Comparison between the scattering profile calculated by Eq. (53) for the clusters composed of the PY hard spheres [the pink profile (4)] and the experimental profile $I_{\mathrm{exp.}}(q)$ [profile (1)] [part (a)]. The calculated polydisperse sphere form factor, $I_{\mathrm{INP}}(q)$ [the red profile (2)], and $I_{\mathrm{HS/inf.}}(q)$ [the blue profile (3)] are also displayed in the figure as references. Presence of the clusters did predict a major part of the excess intensity over the $I_{\mathrm{HS/inf.}}(q)$ observed in Region II. Part (b) highlights a discrepancy between the profile (1) and the profile (4) at 0.6 < q < 1.2 nm^{-1} with the expanded intensity scale and q scale.

This article is copyrighted as indicated in the article. Reuse of AIP content is subject to the terms at: http://scitation.aip.org/termsconditions. Downloaded to IP: 140.110.200.41 On: Fri, 26 Jun 2015 00:57:21

Profile (3) in Figure 5 corresponds to the calculated $I_{HS/inf.}(q)$. It can be seen that this calculated profile did match the experimental profile (1) better than $I_{INP}(q)$ [profile (2)], but there still existed an obvious deviation from $I_{exp.}(q)$ at $q < 1.5$ nm^{-1} in Region I and in the whole q region in Region II, where the observed intensity in Region II was larger than the calculated $I_{HS/inf.}(q)$. Therefore, the hard core potential (Eq. (14)) together with the PY type interparticle interaction (Eq. (13)) cannot account for the observed SAXS profile in Regions I and II.

Profile (4) in Figure 5(a) corresponds to the calculated curve of $I_{HS/cluster}(q)$ for the clusters formed by the PY hard spheres. It can be seen that the inclusion of the concept of the cluster into the PY hard sphere model significantly reduces the discrepancy between the theoretical and experimental scattering profiles; the inclusion of the scattering from the clusters predicted the excess intensity observed in $I_{exp.}(q)$ relative to $I_{HS/inf.}(q)$ in Region II. Nevertheless, an obvious deviation between the calculated and observed intensity profile was still observable in the q range of $0.6 < q < 1.2$ nm^{-1}. This discrepancy is highlighted in Figure 5(b) with the expanded scales. We believe this deviation is caused by the PY model used in the calculation; the interaction between the NPs forming the clusters cannot be described by the hard-core repulsive potential only. As a matter of fact, it is hard to envision why the NPs would form the local clusters, if they interact through the repulsive force only. Thus, the failure of the analysis based on the PY hard-sphere model elucidates an important role of an attractive force in addition to the hard-core repulsive force. To account for the effects of the attractive interparticle interaction on the scattering profile, we shall replace the clusters composed of the PY hard sphere by those composed of the SHS, which is to be presented in Sec. V B.

B. Analysis based on the clusters composed of SHS

Similar to Eq. (53), the scattering intensity from the clusters composed of spheres interacting through the SHS potential is expressed as

$$I_{SHS/cluster}(q) = K_2\{\pi^3 n \left\langle V_p^2\Phi^2(q;R_p)\right\rangle \left\langle V_c^2\Phi^2(q;R_c)\right\rangle + \left\langle V_p^2\Phi^2(q;R_p)\right\rangle [S_{SHS/inf}(q;R_{p,av}) * \left\langle V_c^2\Phi^2(q;R_c)\right\rangle]\}. \quad (54)$$

Figure 6 displays the calculated $I_{SHS/cluster.}(q)$ [profile (4)] using Eq. (54) assuming $u_0 = -2.16k_BT$, $\Delta = 0.2$ nm ($\varepsilon = 0.04$), and the average cluster radius ($\langle R_c\rangle$) of 4.2 nm. The calculated polydisperse sphere form factor, $I_{INP}(q)$ [the red profile (2)], and the intensity profile associated with SHS spheres dispersed in an infinitely large medium $I_{SHS/inf.}(q)$ [the blue profile (3)] were also displayed for comparison. It can be seen that the SHS model offered a better fit than the HS model to the experimental scattering profile [profile (1)] at $q < 1.5$ nm^{-1} in Region I, where the negative deviation found in the $I_{HS/inf.}$ relative to $I_{exp.}$ was not observed in $I_{SHS/inf.}$ (compare profile 3 in Figures 5 and 6). The results clearly indicated the physical significance of the attractive tail in $u(r)$ for the two-body interactions of the particles on the scattering profile in the low-q part in Region I.

With the further inclusion of the effect of cluster formation, the calculated profile $I_{SHS/cluster}(q)$ (i.e., profile 4) was seen to offer a very good fit to the experimental data in Regions I and II at $q > q^* = 0.5$ nm^{-1}, revealing that the primary NPs formed local clusters due to the short-range attraction predicted by the SHS potential. The volume fraction of the particles was assumed to be 0.49. It should be noted that this volume fraction was not the overall volume fraction of the Pd NPs in the whole hybrid, but rather the average local volume fraction of the NPs confined within the clusters.

It is noted that the calculated profile (4) still did not fit with the experimental profile (1) at $q < q^* \cong 0.5$ nm^{-1}. This deviation, which increased with decreasing q, must reflect existence of a higher-order structure of the clusters as a tertiary structure. The scattering from a mass-fractal structure built up by the clusters was thus taken into account on the basis of Eqs. (48)–(50). The analysis of the entire observed SAXS

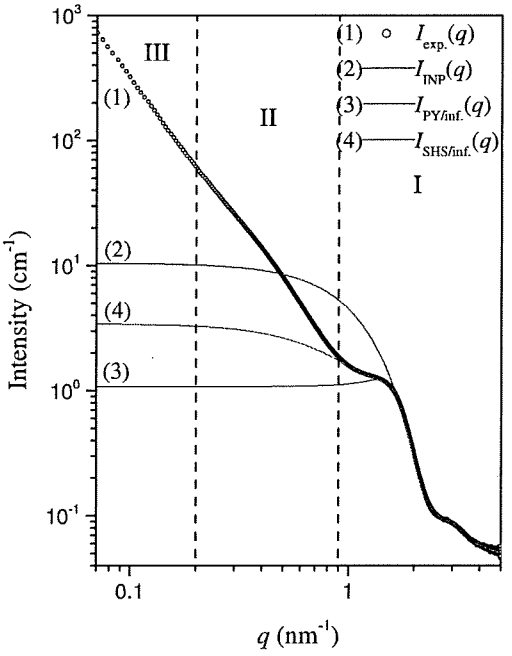

FIG. 6. Comparison between the scattering profile calculated by Eq. (54) [i.e., $I_{SHS/cluster}(q)$, profile (4)] and the experimental profile $I_{exp.}(q)$ [profile (1)]. The calculated profiles of $I_{SHS/inf.}(q)$ [profile (3)] and polydisperse sphere form factor $I_{INP}(q)$ [profile (2)] are also displayed in the figure as references.

This article is copyrighted as indicated in the article. Reuse of AIP content is subject to the terms at: http://scitation.aip.org/termsconditions. Downloaded to IP: 140.110.200.41 On: Fri, 26 Jun 2015 00:57:21

profile using Eq. (48) based on the hierarchical structure model developed here will be presented in Sec. V C.

C. Analysis using the model of the mass-fractal superstructure built up by the clusters composed of SHS

According to Eq. (48), the scattering intensity of a mass-fractal structure formed by the clusters in which the NPs interacting through the SHS potential is expressed as $I_{net}(q) = I_{MF}(q)I_{SHS/cluster}(q)$. Figure 7 presents the calculated SAXS profile on the basis of Eqs. (48)–(50) [profile (5) shown by the red line marked $I_{net}(q)$] with the value of $D_m = 2.3$ and the values for the other relevant parameters which were already estimated by the best-fit between $I_{exp}(q)$ [profile (1)] and $I_{SHS/cluster}(q)$ [profile (3)] at $q \geq q^*$, as also shown in Figure 7. It can be seen that the calculated profile very well fitted with the experimental profile (1) [$I_{exp}(q)$ shown by the unfilled circles] over the entire q range.

The scattering function given by Eqs. (23), (48)–(50), and (54) indeed represents a model for a hierarchical structure with three distinct hierarchical levels. The primary NPs with well-defined spherical geometry and size constituted the first level of the hierarchical structure. These primary NPs interacted through the SHS potential and self-assembled to form the local clusters which represented the second level of the structure. The clusters further self-assembled to build up a larger-scale mass-fractal structure as the structure of the third level.

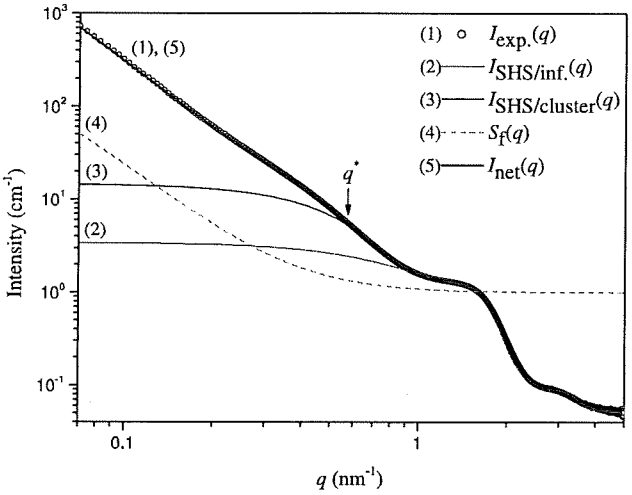

FIG. 7. Comparison between the scattering profile I_{net} calculated by Eqs. (23), (48)–(50), and (54) [profile (5)] and the experimental profile $I_{exp.}(q)$ [profile (1)]. The calculated profiles of $I_{SHS/inf.}(q)$ [profile (2)], $I_{SHS/cluster}(q)$ [profile (3)], and $S_{MF}(q)$ [profile (4)] are also displayed in the figure as references.

VI. DISCUSSION

The foregoing systematic analysis of the SAXS profile revealed the formation of a hierarchical structure with the three levels. A schematic illustration of the hierarchical structure elucidated hereby is shown in Figure 8(a). The presented hierarchical structure was indeed quite universal for various hybrid systems studied in this work, e.g., for those prepared by changing the reduction temperature of the salt for a given set of the other experimental variables, as demonstrated in Figure 8(b). All the scattering profiles were found to exhibit the universal feature; the three characteristic regions [I] to [III] were identified as in the case for the reduction temperature at 100 °C. All the SAXS profiles were hence fitted by the hierarchical structure model given by Eqs. (48)–(50). The best-fitted results are displayed by the solid red curves in Figure 8(b). It can be seen that the model very well fitted all scattering profiles. There are several fitting parameters as summarized in Table I. However, each fitting parameter or each set of fitting parameters selectively controls the

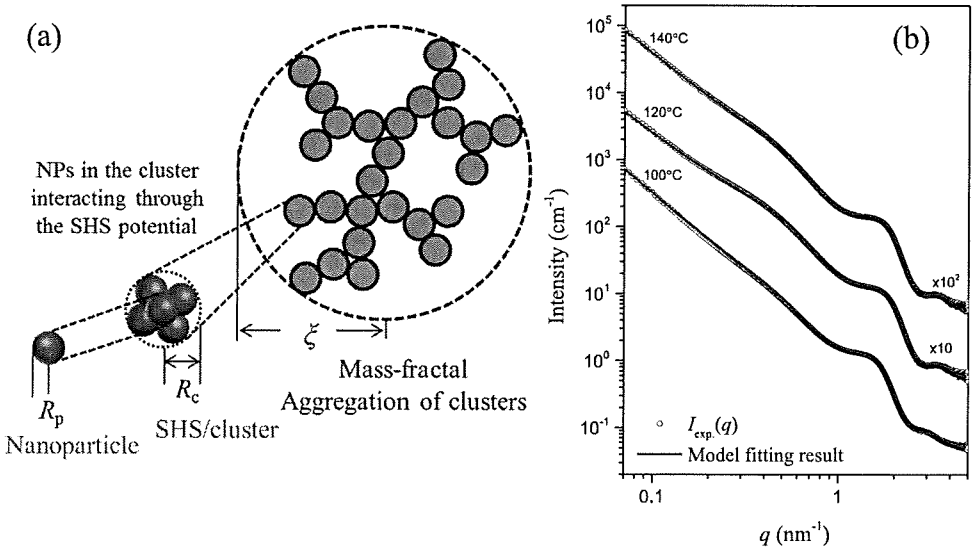

FIG. 8. (a) Schematic illustration of the hierarchical structure composed of three levels formed in the nanocomposites. The upper cutoff size of the fractal structure ξ exists beyond the small q-limit covered by this experiment. (b) SAXS profiles of the hybrids prepared under different reduction temperatures indicated in the figure. All scattering profiles were found to exhibit the same features and were fitted very well by the hierarchical structure model predicted by Eqs. (48)–(50), and (54).

This article is copyrighted as indicated in the article. Reuse of AIP content is subject to the terms at: http://scitation.aip.org/termsconditions. Downloaded to IP: 140.110.200.41 On: Fri, 26 Jun 2015 00:57:21

TABLE I. Structural parameters evaluated from the fits which characterize the hierarchical structure composed of three levels.

	Primary structure (level one)		Secondary structure (level two)					Tertiary structure (level three)	
$T_{red.}$ (°C)	$\langle R_p \rangle$ (nm)	P_p	$\langle R_c \rangle$ (nm)	P_c	ϕ	Δ (Å)	u_0	D_m	ξ (nm)
100	1.8 ± 0.012	0.16 ± 0.023	4.2 ± 0.21	0.01 ± 0.011	0.491 ± 0.021	2.1	$-2.2k_BT$	2.3	200 ± 72
120	1.7 ± 0.011	0.16 ± 0.011	4.1 ± 0.22	0.01 ± 0.007	0.497 ± 0.014	2.1	$-2.2k_BT$	2.2	200 ± 52
140	1.7 ± 0.008	0.14 ± 0.011	4.2 ± 0.17	0.01 ± 0.004	0.501 ± 0.015	2.1	$-2.1k_BT$	2.3	200 ± 63

scattering function in different q regions (regions I to III), i.e., in different hierarchical structure levels. Even the many parameters associated with the secondary structure affect the scattering function in Region II in somewhat different ways and in different q windows within Region II, which makes this model very useful as a predictive one. Table I lists the numerical values of the structure parameters obtained from the fitting, which include those characterizing the hierarchical structure composed of the three levels: the average radius of the primary NPs ($\langle R_p \rangle$) and its polydispersity (P_p) for level one, the average radius of clusters ($\langle R_c \rangle$) and its polydispersity (P_c), the local volume fraction of the NPs within the clusters (ϕ), the depth of attractive potential (u_0) in the SHS, the width of SHS potential well (Δ) for level two, the mass fractal dimension of the large-length-scale fractal structure (D_m), and the upper cutoff size ξ for level three. The parameters obtained do not so much depend on $T_{red.}$ obviously; thus, we discuss physical significances of the data taken at $T_{red.} = 100\,°C$ below.

The number-average radii of the primary Pd NPs ($\langle R_p \rangle$) and the clusters ($\langle R_c \rangle$) were ~1.8 and 4.2 nm, respectively. The value $\langle R_p \rangle \sim 1.8$ nm is found to be consistent with the number-average radius NPs measured by the TEM (~2.0 nm). Knowing that the local volume fraction of NPs within the clusters was ~0.49, the number of NPs per cluster can be calculated by $N_p = \phi(\langle R^3_c \rangle / \langle R^3_p \rangle) \sim 6$. Therefore, each cluster was formed by the association of about six NPs via SHS interactions having the attractive potential well. The width of the SHS attractive potential well given by Δ was ~0.2 nm, attesting that the attractive interaction was indeed short-ranged. The strength of the attractive interaction characterized by u_0 was about $-2.2k_BT$. The attractive interaction between the NPs may originate from the van der Waals forces between the NPs, the kinetically trapped bridging between the NPs by the P2VP chains adsorbed on their surfaces, and the depletion interaction[41] driven by the conformational entropy loss of free P2VP chains in a narrow interstitial space between NPs.

The low-q intensity profile in Region III was contributed mainly by the mass-fractal structure formed by the aggregation of the clusters. The fractal dimension ~2.3 was close to that predicted by the diffusion-limited cluster-cluster aggregation.[42,43] The upper cutoff length ξ of the fractal structure tends to cause the low-q upturn of $S_{MF}(q)$ to level off from the power law of q^{-D_m} with decreasing q close to $q_\xi \equiv 2\pi/\xi$. However, the profiles shown in Figure 8 apparently indicate that the q range covered did not yet approach the low-q range close to q_ξ, so that the values of ξ shown in Table I determined by the best fit between the theoretical and experimental profiles were subjected to large errors.

It is intriguing to note that the building block of the mass-fractal structure is not the NPs themselves as the primary structure but rather is the clusters as the secondary structure which is composed of several NPs. The same phenomenon was also found for the carbon black (CB) NPs dispersed in the poly(styrene-*ran*-butadiene) (SBR) rubber matrix.[26,44] Note that the so-called "dispersible units" (see Figure 13 in Ref. 26) correspond to the clusters discussed herein. It is crucial to explore the universality of this phenomenon and the physical origin of the cluster formation which is seemingly attributed to the attractive interactions among the NPs.

Moreover, the scattering functions developed in this work are of general use for quantitatively characterizing the morphology of polymer/nanoparticles hybrids. This is because the scattering functions take care a whole spectrum with respect to possible assemblies of the NPs not only the hierarchical structures composed of the three levels [$I_{net}(q)$] but also the interacting NPs dispersed in the infinitely large space [$I_{SHS/inf.}(q)$ and $I_{HS/inf.}(q)$] and the dispersion of the clusters composed of the NPs [$I_{HS/cluster}(q)$ and $I_{SHS/cluster}(q)$]. Thus, the scattering functions can be applied to analyze *in situ* the time-evolution of the hierarchical self-assembly of the NPs during the chemical reduction process of the metal salts. Needless to say, it is crucial to explore, verify, or demonstrate the broad applicability of the model and the scattering functions to other nanoparticles-polymer systems.

VII. CONCLUSIONS

The SAXS profiles of the hybrids of P2VP and Pd NPs prepared by the reduction of $Pd(acac)_2$ were found to be characterized by a hierarchical structure model with the three distinct length scales. The primary NPs with the average diameter of 3.6 nm were first formed, and approximately six NPs subsequently aggregated to form local clusters (with the average diameter of ~8.4 nm) via the short-range SHS interactions between the NPs. It is crucial to note that the attractive-tail potential $u_0 \cong -2.2\ k_BT$ for the inter-nanoparticle interaction is indispensable to account for not only the existence of the clusters of NPs but also the experimental scattering function. The clusters then self-assembled into a large length-scale mass fractal structure with the fractal dimension of ~2.3 through the diffusion-limited aggregation. The hierarchical structure of the NPs formed was found to be universal in the sense that the hierarchical structure having the three characteristic hierarchical levels was always developed at the end of the reduction process, irrespective of the reduction temperature of the salt.

The universal structure is expected to have its physical origin attributed to a self-assembly of the NPs via (a) the

This article is copyrighted as indicated in the article. Reuse of AIP content is subject to the terms at: http://scitation.aip.org/termsconditions. Downloaded to IP: 140.110.200.41 On: Fri, 26 Jun 2015 00:57:21

reduction-reaction-induced "local phase transition"[45] of the NPs in the polymer matrix which causes the local phase separation into the regions rich and poor in the NPs, giving rise to the liquid phase and the gas phase, respectively, and (b) the kinetically arrested growth of the phase-separating structure caused by the mass-fractal aggregation of the clusters. The local phase separation may be induced when the "local concentration" of the NPs, which were kept being created during the chemical reduction process, exceeds a critical concentration controlled by the short-range attractive interaction between the NPs in the polymer matrix.

ACKNOWLEDGMENTS

The authors acknowledge the support of the Ministry of Science and Technology Taiwan, under Grant No. MOST 102-2633-M-007-002 and the Frontier Center of Fundamental and Applied Sciences of Matters of the National Tsing Hua University. We also thank Professor U-Ser Jeng, Dr. Chun-Jen Su, and Wen-Bin Su at the National Synchrotron Radiation Research Center for supporting the X-ray scattering experiments at beamline BL23A1.

APPENDIX: DERIVATIONS OF EQS. (5b) AND (37)

$T(q)$ in Eq. (5a) represents the structure factor for an infinitely large homogeneous medium. This space is practically considered to be the space irradiated by the incident beam in real experimental systems which is large enough compared with structures studied in the systems. In the case when the space irradiated by the incident beam is a rectangular parallelepiped space with lengths L_x along the propagation direction of the incident beam taken along the Ox axis and L_y and L_z along the two orthogonal Oy and Oz axes normal to the Ox axis, $T(q)$ in Eq. (5a), derived on the basis of the assumption valid for a spherically symmetric irradiated volume, should be rewritten as

$$\begin{aligned} T(\mathbf{q}) &= \int_{V_{\mathrm{ir}}} \exp(-i\mathbf{q}\cdot\mathbf{r})\,\mathrm{d}\mathbf{r} \\ &= \int_{-L_x/2}^{L_x/2} e^{-iq_x x}\mathrm{d}x \int_{-L_y/2}^{L_y/2} e^{-iq_y y}\mathrm{d}y \int_{-L_z/2}^{L_z/2} e^{-iq_z z}\mathrm{d}z \\ &= V_{\mathrm{ir}} \frac{\sin(q_x L_x/2)}{(q_x L_x/2)} \frac{\sin(q_y L_y/2)}{(q_y L_y/2)} \frac{\sin(q_z L_z/2)}{(q_z L_z/2)}, \end{aligned} \tag{A1}$$

where $T(\mathbf{q})$ involves the volume integral over the irradiated volume V_{ir}, $V_{ir} = L_x L_y L_z$, and q_k $(k = x,\ y,\ z)$ is the component of $\mathbf{q}$ along the k axis. When $L_x, L_y, L_z \to \infty$, and $V_{ir} \to \infty$, $T(\mathbf{q})$ has a nonzero value only at $q_x = q_y = q_z = 0$ and the value of $T(\mathbf{q} = 0)$ diverges. Thus, $T(\mathbf{q})$ is expressed by using Dirac's delta function $\delta(\mathbf{q})$,

$$\lim_{L_x, L_y, L_z \to \infty} T(\mathbf{q}) = K_3\,\delta(\mathbf{q}), \tag{A2}$$

where K_3 is a proportionality constant, and $\delta(\mathbf{q})$ satisfies

$$\lim_{q\to 0} \delta(\mathbf{q}) = \infty, \quad \int \delta(\mathbf{q})\,\mathrm{d}\mathbf{q} = 1. \tag{A3}$$

From Eqs. (A2) and (A3) K_3 is given by

$$K_3 = \lim_{L_x, L_y, L_z \to \infty} \int T(\mathbf{q})\mathrm{d}\mathbf{q}, \tag{A4}$$

$$\int T(\mathbf{q})d\mathbf{q} = V_{ir} \prod_{i=1}^{3} \int_0^\infty \frac{\sin(q_i L_i/2)}{(q_i L_i/2)} \mathrm{d}q_i \tag{A5}$$

where $i = 1, 2$, and 3 corresponds to x, y, and z, respectively.

By replacing $w_i \equiv q_i L_i/2$ and noting that

$$\int_0^\infty \frac{\sin w_i}{w_i} \mathrm{d}w_i = \frac{\pi}{2},$$

we obtain

$$\int T(\mathbf{q})\mathrm{d}\mathbf{q} = \pi^3 \tag{A6}$$

independent of L_x, L_y, and L_z. Thus, $K_3 = \pi^3$, and Eq. (A2) with $K_3 = \pi^3$ is valid, as long as $L_x, L_y, L_z \to \infty$.

Let us now derive Eq. (37). From Eqs. (2)–(4),

$$S(\mathbf{q}) = N_t[nT(\mathbf{q}) + S_{ZP}(\mathbf{q})]. \tag{A7}$$

Substituting Eq. (A7) into Eq. (36), we obtain

$$\frac{\mathrm{d}\Sigma(\boldsymbol{q})}{\mathrm{d}\Omega} = nP(q)\,[nT(\boldsymbol{q}) * \overset{2}{\tilde{\sigma}}(\mathbf{q}) + S_{ZP}(\mathbf{q}) * \overset{2}{\tilde{\sigma}}(\mathbf{q})], \tag{A8}$$

$$T(\mathbf{q}) * \overset{2}{\tilde{\sigma}}(\mathbf{q}) = \int T(\mathbf{u})\,\overset{2}{\tilde{\sigma}}(\mathbf{q}-\mathbf{u})\,\mathrm{d}\mathbf{u}. \tag{A9}$$

$\int \mathrm{d}\mathbf{u}$ is the volume integration in 3D q space.

$T(\mathbf{u})$ decreases with $|\mathbf{u}|$ much more sharply than $\overset{2}{\tilde{\sigma}}(\mathbf{u})$ does, as predicted by Eq. (A2) and schematically shown in Figure 9(a). Consequently, the product $T(\mathbf{u})\,\overset{2}{\tilde{\sigma}}(\mathbf{q}-\mathbf{u})$ has a nonzero value only when $|\mathbf{u}| \cong 0$, where $\overset{2}{\tilde{\sigma}}(\mathbf{q}-\mathbf{u}) \cong \overset{2}{\tilde{\sigma}}(\mathbf{q})$, a constant value independent of $\mathbf{u}$, as schematically shown in Figure 9(b). Thus, Eq. (A9) is given by

$$\int T(\mathbf{u})\,\overset{2}{\tilde{\sigma}}(\mathbf{q}-\mathbf{u})\mathrm{d}\mathbf{u} \cong \overset{2}{\tilde{\sigma}}(\mathbf{q}) \int T(\mathbf{u})\,\mathrm{d}\mathbf{u} = \pi^3\,\overset{2}{\tilde{\sigma}}(\mathbf{q}). \tag{A10}$$

From Eqs. (A8)–(A10), Eq. (37) can be derived.

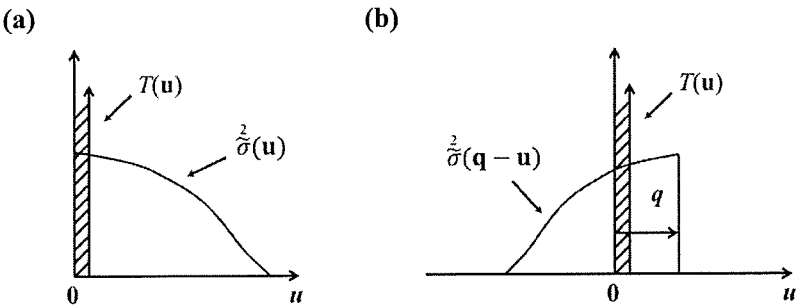

FIG. 9. (a) Properties of two functions, $T(\mathbf{u})$ and $\overset{2}{\tilde{\sigma}}(\mathbf{u})$, and (b) shifting one of the function, e.g., $\overset{2}{\tilde{\sigma}}(\mathbf{u})$ relative to the other $T(\mathbf{u})$ by $\mathbf{q}$. Note that the directions of $\mathbf{q}$ and $\mathbf{u}$ are not necessarily the same as shown in part (b).

This article is copyrighted as indicated in the article. Reuse of AIP content is subject to the terms at: http://scitation.aip.org/termsconditions. Downloaded to IP: 140.110.200.41 On: Fri, 26 Jun 2015 00:57:21

[1]Q. Zhang and L. A. Archer, Langmuir **18**, 10435 (2002).
[2]P. M. Ajayan, L. S. Schadler, and P. V. Braun, *Nanocomposite Science and Technology* (WILEY-VCH, 2003).
[3]I.-Y. Jeon and J.-B. Baek, Materials **3**, 3654 (2010).
[4]G. Kickelbick, Prog. Polym. Sci. **28**, 83 (2003).
[5]J. Jancar, J. F. Douglas, F. W. Starr, S. K. Kumar, P. Cassagnau, A. J. Lesser, S. S. Sternstein, and M. J. Buehler, Polymer **51**, 3321 (2010).
[6]S. K. Kumar, N. Jouault, B. Benicewicz, and T. Neely, Macromolecules **46**, 3199 (2013).
[7]D. R. Paul and L. M. Robeson, Polymer **49**, 3187 (2008).
[8]V. V. Ginzburg, Macromolecules **46**, 9798 (2013).
[9]G. Sandi, R. Kizilel, K. A. Carrado, R. Fernandez-Saavedra, and N. Castagnola, Electrochim. Acta **50**, 3891 (2005).
[10]N. Grossiord, J. Loos, O. Regev, and C. E. Koning, Chem. Mater. **18**, 1089 (2006).
[11]D. Wang, R. Kou, D. Choi, Z. Yang, Z. Nie, J. Li, L. V. Saraf, D. Hu, J. Zhang, G. L. Graff, J. Liu, M. A. Pope, and I. A. Aksay, ACS Nano **4**, 1587 (2010).
[12]A. V. Kyrylyuk, M. C. Hermant, T. Schilling, B. Klumperman, C. E. Koning, and P. van der Schoot, Nat. Nanotechnol. **6**, 364 (2011).
[13]A. C. Balazs, C. Singh, E. Zhulina, and Y. Lyatskaya, Acc. Chem.Res. **32**, 651 (1999).
[14]K. A. Carrado and L. Xu, Chem. Mater. **10**, 1440 (1998).
[15]S. Porel, S. Singh, S. S. Harsha, D. N. Rao, and T. P. Radhakrishnan, Chem. Mater. **17**, 9 (2005).
[16]N. Sakamoto, M. Harda, and T. Hashimoto, Macromolecules **39**, 1116 (2006).
[17]M. Adachi, A. Okuma, E. Sivaniah, and T. Hashimoto, Macromolecules **39**, 7352 (2006).
[18]Y. Zhao, K. Saijo, M. Takenaka, S. Koizumi, and T. Hashimoto, Polymer **50**, 2696 (2009).
[19]Y. Zhao, K. Saijo, M. Takenaka, S. Koizumi, and T. Hashimoto, Macromolecules **42**, 5272 (2009).
[20]Y. Zhao, K. Saijo, and T. Hashimoto, Macromolecules **46**, 957 (2013).
[21]T. Hashimoto, M. Harada, and N. Sakamoto, Macromolecules **32**, 6867 (1999).
[22]A. Okumura, K. Tsutsumi, and T. Hashimoto, Polym. J. **32**, 520 (2000).
[23]U. S. Jeng, C. H. Su, C. J. Su, K. F. Liao, W. T. Chuang, Y. H. Lai, J. W. Chang, Y. J. Chen, Y. S. Huang, M. T. Lee, and K. L. Yu, Macromolecules **45**, 5114 (2012).
[24]G. Beaucage, J. Appl. Crystallogr. **28**, 717 (1995).
[25]A. Guinier and G. Fournet, *Small-Angle Scattering of X-rays* (Wiley, NY, 1955).
[26]T. Koga, T. Hashimoto, M. Takenaka, K. Aizawa, N. Amino, M. Nakamura, D. Yamaguchi, and S. Koizumi, Macromolecules **41**, 453 (2008).
[27]F. Zernike and J. A. Prins, Z. Phys. **41**, 184 (1927).
[28]L. S. Ornstein and F. Zernike, Proc. Acad. Sci. Amsterdam **17**, 793 (1914).
[29]J. K. Percus and G. J. Yevick, Phys. Rev. **110**, 1 (1958).
[30]P. A. Egelstaff, *An Introduction to the Liquid State* (Academic Press, London, New York, 1967), p. 32.
[31]R. J. Baxter, J. Chem. Phys. **49**, 2770 (1968).
[32]R. J. Baxter, Aust. J. Phys. **21**, 563 (1968).
[33]M. C. Wertheim, Phys. Rev. Lett. **10**, 321 (1963).
[34]D. J. Kinning and E. L. Thomas, Macromolecules **17**, 1712 (1984).
[35]In order to develop the scattering model on the basis of the Lennard-Jones (LJ) potential, one must first establish a theoretical formula for the direct correlation function $C(r)$ and/or its Fourier transform $C(q)$ based on the PY closure relation of Eq. (13) in the case when $u(r)$ in Eq. (13) is given by the LJ potential. In this case, neither the analytical solution nor the theoretical formula which enables numerical calculations of the scattering function with a reasonable computation time has been presented yet up to this moment. Thus, the derivation of the theoretical formula of $C(r)$ or $C(q)$ for the LJ potential deserves future works.
[36]S. V. G. Menon, C. Manohar, and K. S. Rao, J. Chem. Phys. **95**, 9186 (1991).
[37]T. Hashimoto, H. Tanaka, S. Koizumi, K. Naka, and Y. Chujo, J. Appl. Crystallogr. **40**, 73 (2007).
[38]S. H. Chen and T. L. Lin, in *Neutron Scattering, Methods of Experimental Physics Part B*, edited by K. Skold and D. L. Price (Academic Press, New York, 1986), Vol. 23.
[39]G. V. Z. Schulz, Z. Phys. Chem. **B30**, 379 (1935).
[40]T. Teixeira, J. Appl. Crystallogr. **21**, 781 (1988).
[41]Y. Mao, M. E. Cates, and H. N. W. Lekkerkerker, Physica A **222**, 10 (1995).
[42]P. Meakin, J. Colloid Interface Sci. **102**, 491 (1984).
[43]T. A. Witten and L. M. Sander, Phys. Rev. B **27**, 5686 (1983).
[44]T. Koga, M. Takenaka, K. Aizawa, M. Nakamura, and T. Hashimoto, Langmuir **21**, 11409–11413 (2005).
[45]If we coarse-grain the matrix for the NPs (P2VP/benzyl alcohol solution) as a gas phase and take an analogy of the NPs to atoms, then the phase transition can be regarded as the gas-liquid phase transition of atoms, which develops regions rich in atoms (a liquid phase) and regions poor in atoms (a gas phase).

This article is copyrighted as indicated in the article. Reuse of AIP content is subject to the terms at: http://scitation.aip.org/termsconditions. Downloaded to IP: 140.110.200.41 On: Fri, 26 Jun 2015 00:57:21